

Article

Mechanical and Anticorrosive Properties of TiNbTa and TiNbTaZr Films on Ti-6Al-4V Alloy

Yung-I Chen ^{1,2,*} , Yi-Jyun Chen ¹, Cheng-Yi Lai ¹ and Li-Chun Chang ^{3,4} 

¹ Department of Optoelectronics and Materials Technology, National Taiwan Ocean University, Keelung 202301, Taiwan

² Center of Excellence for Ocean Engineering, National Taiwan Ocean University, Keelung 202301, Taiwan

³ Department of Materials Engineering, Ming Chi University of Technology, New Taipei 243303, Taiwan

⁴ Center for Plasma and Thin Film Technologies, Ming Chi University of Technology, New Taipei 243303, Taiwan

* Correspondence: yichen@mail.ntou.edu.tw

Abstract: In this study, TiNbTa and TiNbTaZr films were utilized as protective coatings on a Ti-6Al-4V alloy to inhibit corrosive attacks from NaCl aqueous solution and simulated body fluid. The structural and mechanical properties of multicomponent TiNbTa(Zr) films were investigated. The corrosion resistance of the TiNbTa(Zr)-film-modified Ti-6Al-4V alloy was evaluated using potentiodynamic polarization tests in a NaCl aqueous solution. The results indicate that the TiNbTa(Zr) films with high Ti and Zr contents exhibited inferior corrosive resistance related to the films with high Ta and Nb contents. Moreover, the TiNbTa(Zr)-coated Ti-6Al-4V plates were immersed in Ringer's solution for eight weeks; this solution was widely used as a simulated body fluid. The formation of surficial oxide layers above the TiNbTa(Zr) films was examined using transmission electron microscopy and X-ray photoelectron spectroscopy, which prevented the elution of Al and V from the Ti-6Al-4V alloy. Ti₃₃Nb₁₉Ta₂₁Zr₂₇, Ti₁₅Nb₆₈Ta₈Zr₉, and Ti₈Nb₈Ta₇₉Zr₅ films are suggested as preferential candidates for TiNbTa(Zr)/Ti-6Al-4V assemblies applied as biocompatible materials.

Keywords: biocompatible materials; corrosion resistance; mechanical properties



Citation: Chen, Y.-I.; Chen, Y.-J.; Lai, C.-Y.; Chang, L.-C. Mechanical and Anticorrosive Properties of TiNbTa and TiNbTaZr Films on Ti-6Al-4V Alloy. *Coatings* **2022**, *12*, 1985. <https://doi.org/10.3390/coatings12121985>

Academic Editors: Ioana Demetrescu and Anca Mazare

Received: 17 November 2022

Accepted: 15 December 2022

Published: 18 December 2022

Publisher's Note: MDPI stays neutral with regard to jurisdictional claims in published maps and institutional affiliations.



Copyright: © 2022 by the authors. Licensee MDPI, Basel, Switzerland. This article is an open access article distributed under the terms and conditions of the Creative Commons Attribution (CC BY) license (<https://creativecommons.org/licenses/by/4.0/>).

1. Introduction

The development of biocompatible long-term implants without evident side effects has attracted the interest of researchers [1,2]. The literature indicates that high strength, high-wear resistance, and low Young's modulus are the crucial requirements for orthopedic long-term implantation [3,4]. Among these material characteristics, low Young's modulus is the essential property preventing the "stress shielding" effect [5]. In contrast to periprosthetic bone with a Young's modulus less than 30 GPa [6], the stiffer artificial implants endure the majority of the load, resulting in bone resorption accompanied with porous constructions [7–9]. Ti-base alloys with a low Young's modulus were utilized as implants [6]. Ti-6Al-4V has been widely used in medical applications due to its excellent mechanical properties, corrosion resistance, and biocompatibility [10–12]. However, the eluted toxic ions, aluminum and vanadium, could cause undesirable neurological disorders, Alzheimer's disease, and local inflammation in the biological system [13], and the elution behavior needs to be inhibited. Ti-based alloys comprise two distinct crystalline structures, α -phase and β -phase, which are hexagonal close-packed (hcp) and body-centered cubic (bcc) phases [14], respectively. Nb, Ta, and Mo are recognized as β -phase stabilizers for Ti-alloys and β -phase Ti-alloys exhibit lower Young's modulus and higher strength related to those of α -phase Ti-alloys [14–16]. TiNbTa [3], TiNbZrTa, and TiMoZrTa [14] alloys have been proposed as alternatives for biocompatible materials. Ti, Nb, and Ta elements, as well as Zr, Ru, Sn, and Au, exhibit exceptional biocompatibility in the human body [17]. Moreover, TiNbTa alloys have been shown to exhibit excellent corrosion resistance in contrast to

the Ti-6Al-4V alloy due to the formation of a passivation oxide film consisting of Nb₂O₅ and Ta₂O₅; therefore, TiNbTa alloys without the elution effect of Al and V ions have been proposed as candidates for orthopedic implants [3].

Combining TiTaNb films and a commercial Ti-6Al-4V alloy has been recommended for application as implants [18]; however, the number of investigations into the aforementioned combination is limited. Lai et al. [19] have reported that TiNbZr and TiNbZrTa films fabricated through cathodic arc evaporation assisted the survival and growth of cells and were applied for orthopedic or dental implants. TiTaHfNbZr high-entropy alloy films prepared on Ti-6Al-4V have been explored [20,21], and these TiTaHfNbZr films exhibited an amorphous structure. This study aimed to evaluate the feasibility of TiNbTa(Zr)/Ti-6Al-4V assembly for implant materials. The low- and medium-entropy TiNbTa(Zr) films were fabricated through co-sputtering. The chemical compositions of TiNbTa(Zr) films were adjusted by distinct sputter powers applied to these targets. The phase structures and mechanical properties of the TiNbTa(Zr) films were studied. The elemental effects on the corrosion resistance of TiNbTa(Zr) films in NaCl solutions and the stability of TiNbTa(Zr) films in Ringer's solution were explored.

2. Materials and Methods

TiNbTa(Zr) films were deposited on p-type (100) silicon wafers and Ti-6Al-4V coupons through co-sputtering with targets of pure Ti, Nb, Ta, and Zr. The sputtering apparatus is described in [22]. The Ti-6Al-4V coupons with dimensions of 20 × 20 × 3 mm³ were grounded and polished before deposition. The substrates were sputtered with a Ti interlayer for enhancing the adhesion between the TiNbTa(Zr) films and substrates. Then, various powers presented in Table 1 were set for co-sputtering TiNbTa and TiNbTaZr films with sputtering times of 50 and 90 min, respectively. The base pressure of the sputtering chamber was below 4 × 10⁻⁵ Pa, whereas the working pressure was set at 1.6 × 10⁻¹ Pa under a 20 sccm flow of pure Ar. The substrate holder was rotated at a speed of 30 rpm during the co-sputtering process in order to homogenize the films' compositions. These films were further immersed in a Ringer's solution, a simulated body fluid, at 37 °C for eight weeks to evaluate the elution test.

Table 1. Co-sputtering parameters and chemical compositions of TiNbTa and TiNbTaZr films.

Sample	Sputter Power (W)				Chemical Composition (at.%)					ΔS_{mix} ¹ (R)
	P_{Ti}	P_{Nb}	P_{Ta}	P_{Zr}	Ti	Nb	Ta	Zr	O	
Ti ₈₃ Nb ₁₀ Ta ₇	200	20	10	—	76.3 ± 0.5	9.3 ± 0.1	6.9 ± 0.0	—	7.5 ± 0.4	0.58
Ti ₃₈ Nb ₃₀ Ta ₃₂	180	80	70	—	36.4 ± 0.1	28.5 ± 0.1	30.1 ± 0.1	—	5.0 ± 0.1	1.09
Ti ₁₀ Nb ₈₀ Ta ₁₀	30	200	20	—	9.2 ± 0.1	76.2 ± 0.3	10.0 ± 0.0	—	4.6 ± 0.4	0.64
Ti ₁₂ Nb ₄ Ta ₈₄	70	20	200	—	10.9 ± 0.2	4.2 ± 0.6	78.2 ± 1.3	—	6.7 ± 2.0	0.54
Ti ₆₁ Nb ₁₃ Ta ₁₁ Zr ₁₅	200	30	20	30	61.3 ± 0.5	12.6 ± 0.2	11.3 ± 0.3	14.8 ± 0.0	—	1.09
Ti ₃₃ Nb ₁₉ Ta ₂₁ Zr ₂₇	180	80	70	140	32.8 ± 0.2	18.9 ± 0.1	21.0 ± 0.3	27.3 ± 0.1	—	1.36
Ti ₁₅ Nb ₆₈ Ta ₈ Zr ₉	70	200	20	30	14.5 ± 0.3	68.2 ± 0.3	8.1 ± 0.4	9.2 ± 0.2	—	0.96
Ti ₁₉ Nb ₁₀ Ta ₉ Zr ₆₂	70	30	200	30	19.1 ± 0.2	10.5 ± 0.1	8.5 ± 0.0	61.9 ± 0.1	—	1.06
Ti ₈ Nb ₈ Ta ₇₉ Zr ₅	70	30	20	200	7.6 ± 0.2	8.1 ± 0.1	78.9 ± 0.6	5.4 ± 0.6	—	0.74

¹ ΔS_{mix} : Mixing entropy.

The chemical compositions of the TiNbTa(Zr) films were examined using a field-emission electron probe microanalyzer (JXA-iHP200F, JEOL, Akishima, Japan). The phase constitutions of the films were confirmed using an X-ray diffractometer (XRD, X'Pert PRO MPD, PANalytical, Almelo, The Netherlands) under the grazing incident mode. The lattice constants, a_0 , of cubic phases were evaluated according to the following equation [23]:

$$a = a_0 + K \times \frac{\cos^2 \theta}{\sin \theta} \quad (1)$$

where a is the lattice constant of the individual reflection, θ is the diffraction angle, and K is a constant. The grain sizes of the films were evaluated on the basis of a Bragg–Brentano scan (θ – 2θ scan) mode by using the Scherrer formula [23]:

$$D = \frac{0.9\lambda}{f_i \cos \theta_B} \quad (2)$$

where D is the average grain size, β is the full width at half maximum (FWHM) of reflection, θ_B is the Bragg angle, and λ is the X-ray wavelength.

The nanostructures of these films with protective C and Pt layers, prepared using a focused ion beam system (NX2000, Hatachi, Tokyo, Japan), were observed by transmission electron microscopy (TEM, JEM-2010E, JEOL, Akishima, Japan). The hardness and Young's modulus values of the films were measured using a nanoindentation tester (TI-900 Triboindenter, Hysitron, Minneapolis, MN, USA) with a depth of 70 nm. The corrosion behavior of the TiNbTa(Zr) films and bare Ti-6Al-4V coupons were evaluated via potentiodynamic polarization tests (SP-200, BioLogic, Seyssinet-Pariset, France) in a 3.5 wt.% NaCl aqueous solution within a potential range of -2.5 V to 2.5 V. The compositional depth profiles and bonding characteristics of the films and bare Ti-6Al-4V alloy after immersing in Ringer's solution were analyzed using X-ray photoelectron spectroscopy (XPS; PHI 1600, PHI, Kanagawa, Japan). The surface wettability of the films was evaluated by water contact angle measurements.

3. Results and Discussion

3.1. Chemical Compositions and Phase Structures

Table 1 shows the co-sputtering parameters and chemical compositions of the prepared ternary TiNbTa and quaternary TiNbTaZr films. These alloys, with mixing entropy ranging from 0.54 to 1.36 R, are considered low- and medium-entropy alloys. The ternary TiNbTa films included a near-equiatomic $\text{Ti}_{38}\text{Nb}_{30}\text{Ta}_{32}$, a Ti-enriched $\text{Ti}_{83}\text{Nb}_{10}\text{Ta}_7$, an Nb-enriched $\text{Ti}_{10}\text{Nb}_{80}\text{Ta}_{10}$, and a Ta-enriched $\text{Ti}_{12}\text{Nb}_4\text{Ta}_{84}$ film. Figure 1a displays the XRD patterns of the TiNbTa films deposited on Ti-6Al-4V substrates. The $\text{Ti}_{83}\text{Nb}_{10}\text{Ta}_7$ film exhibited a mixed hcp and bcc phase, whereas the $\text{Ti}_{38}\text{Nb}_{30}\text{Ta}_{32}$, $\text{Ti}_{10}\text{Nb}_{80}\text{Ta}_{10}$, and $\text{Ti}_{12}\text{Nb}_4\text{Ta}_{84}$ films exhibited a bcc structure. The valence electron concentration (VEC) is an indicator for forecasting the crystalline phases of solid solutions in high entropy alloys [24,25]. The VEC values were 4.17, 4.61, 4.90, and 4.88 for the $\text{Ti}_{83}\text{Nb}_{10}\text{Ta}_7$, $\text{Ti}_{38}\text{Nb}_{30}\text{Ta}_{32}$, $\text{Ti}_{10}\text{Nb}_{80}\text{Ta}_{10}$, and $\text{Ti}_{12}\text{Nb}_4\text{Ta}_{84}$ films, respectively. Guo et al. [24] reported that bcc phases were stable as the VEC of alloys was less than 6.87, whereas Yuan et al. [25] have reported that a single bcc or hcp phase was stable as $\text{VEC} > 4.18$ and < 4.09 , respectively, and a mixed bcc and hcp structure formed as $4.09 \leq \text{VEC} < 4.18$. In this study, the VEC of $\text{Ti}_{83}\text{Nb}_{10}\text{Ta}_7$ film was 4.17, and it formed a mixed bcc and hcp phase, whereas the other three ternary films were stable in a bcc phase. Figure 2a displays the cross-sectional TEM (XTEM) image of the $\text{Ti}_{83}\text{Nb}_{10}\text{Ta}_7$ film, which exhibits a typical columnar structure. The selected area electron diffraction (SAED) pattern indicates the coexistence of bcc and hcp phases (Figure 2b). Figure 2c shows the high-resolution TEM (HRTEM) image around the interface between the $\text{Ti}_{83}\text{Nb}_{10}\text{Ta}_7$ film and C protective layer. As shown in the figure, the $\text{Ti}_{83}\text{Nb}_{10}\text{Ta}_7$ film is crystalline, and the selected regions exhibit lattice fringes with d -spacing values of 0.234–0.235 nm in respect of bcc (110) planes. The lattice constants of the bcc phase in $\text{Ti}_{83}\text{Nb}_{10}\text{Ta}_7$, $\text{Ti}_{38}\text{Nb}_{30}\text{Ta}_{32}$, $\text{Ti}_{10}\text{Nb}_{80}\text{Ta}_{10}$, and $\text{Ti}_{12}\text{Nb}_4\text{Ta}_{84}$ films were determined to be 0.3303, 0.3289, 0.3300, and 0.3310 nm, respectively. The near-equiatomic $\text{Ti}_{38}\text{Nb}_{30}\text{Ta}_{32}$ film possessed low lattice constants, whereas the Ta-enriched $\text{Ti}_{12}\text{Nb}_4\text{Ta}_{84}$ film exhibited large lattice constants. On the other hand, the quaternary TiNbTaZr films were categorized as a near-equiatomic $\text{Ti}_{33}\text{Nb}_{19}\text{Ta}_{21}\text{Zr}_{27}$ film, a Ti-enriched $\text{Ti}_{61}\text{Nb}_{13}\text{Ta}_{11}\text{Zr}_{15}$ film, an Nb-enriched $\text{Ti}_{15}\text{Nb}_{68}\text{Ta}_8\text{Zr}_9$ film, a Zr-enriched $\text{Ti}_{19}\text{Nb}_{10}\text{Ta}_9\text{Zr}_{62}$ film, and a Ta-enriched $\text{Ti}_8\text{Nb}_8\text{Ta}_7\text{Zr}_5$ film. The low VEC values of 4.24 and 4.19 for the $\text{Ti}_{61}\text{Nb}_{13}\text{Ta}_{11}\text{Zr}_{15}$ and $\text{Ti}_{19}\text{Nb}_{10}\text{Ta}_9\text{Zr}_{62}$ films, respectively, imply the formation of a mixed bcc and hcp structure, which agrees with their XRD patterns (Figure 1b). In contrast, the $\text{Ti}_{33}\text{Nb}_{19}\text{Ta}_{21}\text{Zr}_{27}$, $\text{Ti}_{15}\text{Nb}_{68}\text{Ta}_8\text{Zr}_9$, and $\text{Ti}_8\text{Nb}_8\text{Ta}_7\text{Zr}_5$ films exhibited VEC

values of 4.40, 4.76, and 4.87, respectively, and these films displayed a single bcc phase. The lattice constants of the bcc phase in $\text{Ti}_{33}\text{Nb}_{19}\text{Ta}_{21}\text{Zr}_{27}$, $\text{Ti}_{15}\text{Nb}_{68}\text{Ta}_8\text{Zr}_9$, and $\text{Ti}_8\text{Nb}_8\text{Ta}_{79}\text{Zr}_5$ films were determined to be 0.3368, 0.3322, and 0.3332 nm, respectively. If Vegard's law is obeyed [23], the lattice constants of a solid solution can be calculated using the rule of mixture. The lattice constants of bcc Ti, Nb, Ta, and Zr are 0.332 [26,27], 0.33066 (International Center for Diffraction Data (ICDD) 00-035-0789), 0.33058 (ICDD 00-004-0788), and 0.35453 (ICDD 00-034-0657) nm, respectively. Figure 3 displays the relationship between the measured and calculated lattice constants of the bcc phases of the TiNbTa(Zr) films with a single bcc phase only, which shows a linear variation tendency. The fitted line slope of the measured to the calculated values was 0.9985.

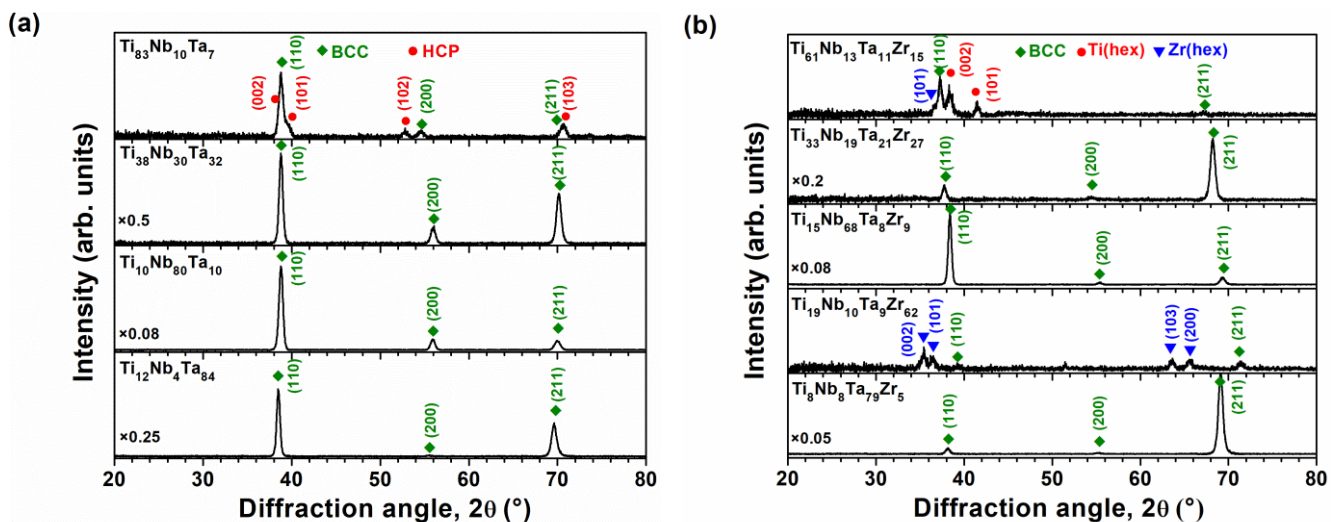


Figure 1. XRD patterns of (a) TiNbTa and (b) TiNbTaZr films.

3.2. Mechanical Properties

Table 2 lists the hardness (H) and Young's modulus (E) of the Ti-6Al-4V substrate and TiNbTa(Zr) films. The H and E of the Ti-6Al-4V coupon were 4.9 and 124 GPa, respectively. A Young's modulus of 110 GPa was reported for Ti-6Al-4V alloy [28]. TiNbSn [28] and TiNbTaZr [6] alloys with low Young's modulus values of 40 and 60 GPa, respectively, were developed as alternative biocompatible materials. However, with the mechanisms of grain boundary strengthening and solid solution strengthening, metallic alloy films exhibit mechanical properties superior to those of bulk alloys [29]. The grain sizes evaluated from the FWHMs of (110) reflections in Bragg–Brentano XRD patterns were 21, 37, 24, and 32 nm for the $\text{Ti}_{83}\text{Nb}_{10}\text{Ta}_7$, $\text{Ti}_{38}\text{Nb}_{30}\text{Ta}_{32}$, $\text{Ti}_{10}\text{Nb}_{80}\text{Ta}_{10}$, and $\text{Ti}_{12}\text{Nb}_4\text{Ta}_{84}$ films, respectively, and 22, 33, 34, 33, and 38 nm for the $\text{Ti}_{61}\text{Nb}_{13}\text{Ta}_{11}\text{Zr}_{15}$, $\text{Ti}_{61}\text{Nb}_{13}\text{Ta}_{11}\text{Zr}_{15}$, $\text{Ti}_{15}\text{Nb}_{68}\text{Ta}_8\text{Zr}_9$, $\text{Ti}_{19}\text{Nb}_{10}\text{Ta}_9\text{Zr}_{62}$, and $\text{Ti}_8\text{Nb}_8\text{Ta}_{79}\text{Zr}_5$ films, respectively. Because these films exhibited various compositions, the relationship between hardness and grain size could not be interpreted by the normal or inverse Hall–Petch strengthening (grain boundary strengthening) mechanism. The H values were 4.0, 4.3, 11.7, and 6.9 GPa for hcp-Ti, bcc-Nb, bcc-Ta, and hcp-Zr films, respectively. The films with high Ta content should have high H values. $\text{Ti}_{12}\text{Nb}_4\text{Ta}_{84}$ and $\text{Ti}_8\text{Nb}_8\text{Ta}_{79}\text{Zr}_5$ films exhibited maximum hardness values of 7.7 and 12.1 GPa among the ternary and quaternary films, respectively, which implies that the solid solution strengthening mechanism dominated the hardness of these TiNbTa(Zr) films. As shown in Table 2, the TiNbTa(Zr) films with a single bcc phase exhibited high E values of 142–226 GPa, whereas the films with a mixture of bcc and hcp phases exhibited low E values of 108–115 GPa. This variation was not consistent with that reported for bulk Ti alloys, i.e., β (bcc)-phase Ti-alloys that exhibited low Young's modulus. Though these TiNbTa(Zr) films exhibited high E values, these films should not cause a stress-shielding effect due to the low volume ratios of film-to-bulk Ti-6Al-4V. Moreover, selected TiNbTa(Zr) films improved the toughness and resistance to plastic deformation represented by high

H/E [30] and H^3/E^2 [31] indicators, respectively. The $Ti_{12}Nb_4Ta_{84}$ and $Ti_8Nb_8Ta_{79}Zr_5$ films exhibited favorable H/E and H^3/E^2 values in the studied ternary and quaternary films, respectively.

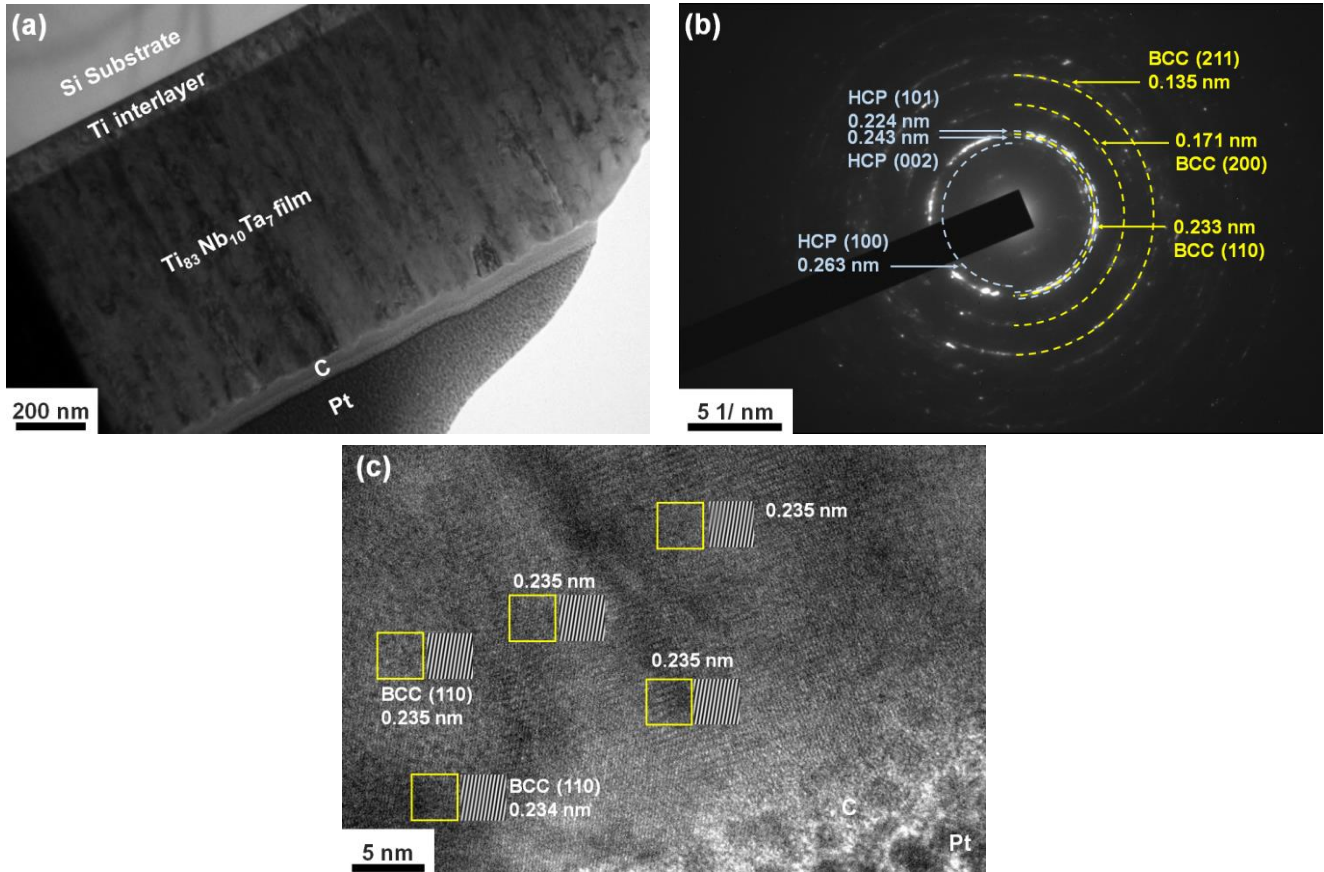


Figure 2. (a) XTEM image, (b) SAED pattern, and (c) HRTEM image of the $Ti_{33}Nb_{10}Ta_7$ film prepared on Si substrate.

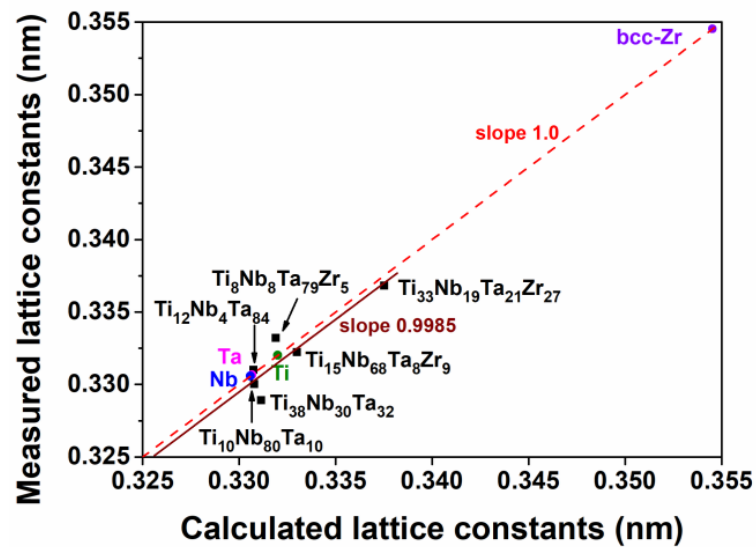


Figure 3. Relationship between the measured and calculated lattice constants of the bcc phases of the TiNbTa(Zr) films.

Table 2. Mechanical properties of TiNbTa and TiNbTaZr films.

Sample	H^1 (GPa)	E^2 (GPa)	H/E	H^3/E^2 (GPa)
Ti-6Al-4V	4.9 ± 0.4	124 ± 8	0.040	0.008
Ti ₈₃ Nb ₁₀ Ta ₇	2.7 ± 0.3	110 ± 7	0.025	0.002
Ti ₃₈ Nb ₃₀ Ta ₃₂	5.0 ± 0.2	150 ± 10	0.033	0.006
Ti ₁₀ Nb ₈₀ Ta ₁₀	4.2 ± 0.5	142 ± 8	0.030	0.004
Ti ₁₂ Nb ₄ Ta ₈₄	7.7 ± 0.3	216 ± 6	0.036	0.010
Ti ₆₁ Nb ₁₃ Ta ₁₁ Zr ₁₅	3.9 ± 1.0	108 ± 17	0.036	0.005
Ti ₃₃ Nb ₁₉ Ta ₂₁ Zr ₂₇	5.9 ± 0.9	163 ± 12	0.036	0.008
Ti ₁₅ Nb ₆₈ Ta ₈ Zr ₉	9.6 ± 1.1	165 ± 14	0.058	0.032
Ti ₁₉ Nb ₁₀ Ta ₉ Zr ₆₂	7.0 ± 0.3	115 ± 4	0.061	0.026
Ti ₈ Nb ₈ Ta ₇₉ Zr ₅	12.1 ± 1.0	226 ± 9	0.054	0.035

¹ H : Hardness; ² E : Young's modulus.

3.3. Corrosion Resistance

Figure 4 depicts the potentiodynamic polarization curves of TiNbTa and TiNbTaZr films and the uncoated Ti-6Al-4V substrate as immersed in a 3.5 wt.% NaCl aqueous solution. The corrosion potential (E_{corr}) and corrosion current density (I_{corr}) values, determined by the Tafel extrapolation method, are presented in Table 3. The polarization resistance (R_p) values of the samples were determined according to the Stern–Geary equation [32]. The R_p values of TiNbTa films ranged from 4.1×10^3 to 1.5×10^4 $\text{K}\Omega\text{cm}^2$, whereas the R_p values of TiNbTaZr films were in the range of 5.3×10^3 – 2.9×10^4 $\text{K}\Omega\text{cm}^2$. Although there are no significant pitting behaviors for Ti₈₃Nb₁₀Ta₇ and Ti₆₁Nb₁₃Ta₁₁Zr₁₅, it is noteworthy that the ternary and quaternary Ti-enriched films have the R_p values of 4.1 and 5.3×10^3 $\text{K}\Omega\text{cm}^2$, respectively. These R_p values are similar to the bare Ti-6Al-4V of 4.5×10^3 $\text{K}\Omega\text{cm}^2$, which confirmed that the Ti-enriched films had inferior corrosion resistance in NaCl solution in relation to the other TiNbTa(Zr) films. The enhancement of R_p values caused by adding Zr into ternary TiNbTa films is evident. For example, the R_p ratio of Ti-enriched Ti₈₃Nb₁₀Ta₇ related to the bare Ti-6Al-4V was 0.9, whereas that of the Ti-enriched Ti₆₁Nb₁₃Ta₁₁Zr₁₅ was 1.2. Moreover, the R_p ratio increased from 1.7 for the Nb-enriched Ti₁₀Nb₈₀Ta₁₀ to 4.3 for the Nb-enriched Ti₁₅Nb₆₈Ta₈Zr₉. Additionally, the R_p ratio increased from 3.3 for the Ta-enriched Ti₁₂Nb₄Ta₈₄ to 4.3 for the Ta-enriched Ti₈Nb₈Ta₇₉Zr₅. The change in corrosion resistance was associated with the fact that ZrO₂ has the more negative Gibbs free energy per mole of O₂ among the available four oxides ZrO₂, TiO₂, Ta₂O₅, and Nb₂O₅, implying that the passivation film becomes thicker with an increase in Zr content [33]. Therefore, the I_{corr} of quaternary films was lower than that of ternary films, resulting in higher corrosion resistance.

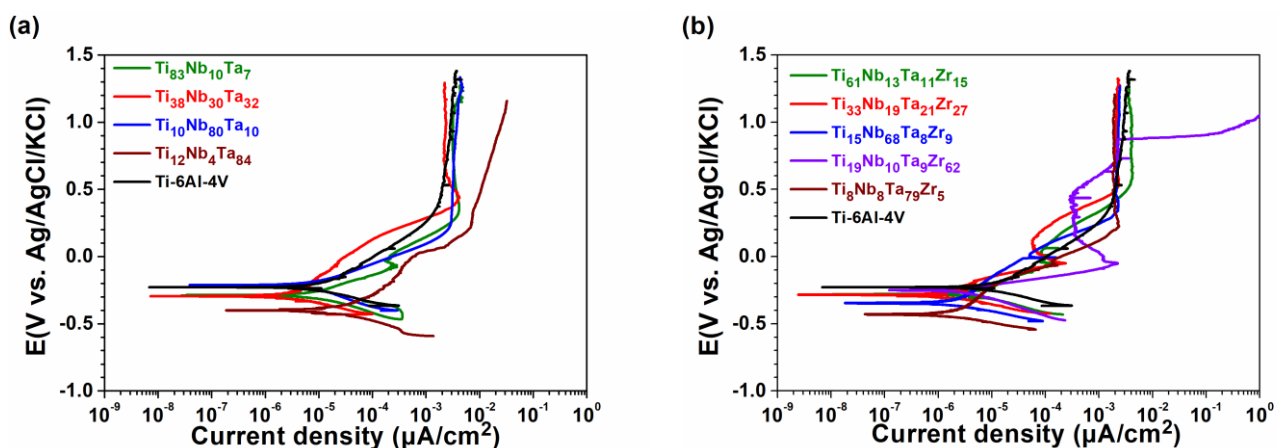


Figure 4. Potentiodynamic polarization curves of (a) TiNbTa and (b) TiNbTaZr films and the Ti-6Al-4V substrate in a 3.5 wt.% NaCl aqueous solution.

Table 3. Corrosion characteristics of the Ti-6Al-4V substrate and TiNbTa(Zr) films.

Sample	E_{corr} (mV)	I_{corr} ($\mu\text{A}/\text{cm}^2$)	R_p ($\text{K}\Omega\text{cm}^2$)	R_p Ratio
Ti-6Al-4V	−250	0.004	4.5×10^3	1.0
Ti ₈₃ Nb ₁₀ Ta ₇	−268	0.006	4.1×10^3	0.9
Ti ₃₈ Nb ₃₀ Ta ₃₂	−315	0.002	8.8×10^3	2.0
Ti ₁₀ Nb ₈₀ Ta ₁₀	−214	0.003	7.6×10^3	1.7
Ti ₁₂ Nb ₄ Ta ₈₄	−375	0.001	1.5×10^4	3.3
Ti ₆₁ Nb ₁₃ Ta ₁₁ Zr ₁₅	−308	0.005	5.3×10^3	1.2
Ti ₃₃ Nb ₁₉ Ta ₂₁ Zr ₂₇	−281	0.001	2.9×10^4	6.4
Ti ₁₅ Nb ₆₈ Ta ₈ Zr ₉	−365	0.001	2.1×10^4	4.7
Ti ₁₉ Nb ₁₀ Ta ₉ Zr ₆₂	−247	0.002	7.7×10^3	1.7
Ti ₈ Nb ₈ Ta ₇₉ Zr ₅	−441	0.001	1.9×10^4	4.2

The Ti₃₃Nb₁₉Ta₂₁Zr₂₇ film and the bare Ti-6Al-4V exhibited E_{corr} values of −281 and −250 mV, respectively. The Ti₃₃Nb₁₉Ta₂₁Zr₂₇ film exhibited a more negative corrosion potential value than that of bare Ti-6Al-4V and had the highest R_p of $2.9 \times 10^4 \text{ K}\Omega\text{cm}^2$ or R_p ratio of 6.4 in this study. The increasing corrosion resistance of Ti₃₃Nb₁₉Ta₂₁Zr₂₇ can be attributed to the formation of amorphous films comprising Ta₂O₅, Nb₂O₅, and ZrO₂ on the free surface. These aforementioned dense and stable passive oxide layers can restrict the electrochemical reactions, leading to a decrease in corrosion current density [18]. However, the Ti₁₉Nb₁₀Ta₉Zr₆₂ film with the highest Zr content in this study exhibited current fluctuations in its potentiodynamic polarization curve similar to that observed for the uncoated Ti-6Al-4V (Figure 4), implying the conduct of pitting behavior. According to the previous literature [34,35], the possible explanation for the pitting behavior can be ascribed to the presence of chloride ions in NaCl solution. The aggressive Cl ions with high electronegativity can easily combine with oxygen vacancies in the passive layer, which results in the formation of localized pitting corrosion at the grain boundaries and induces the formation of a porous structure. Moreover, the galvanic corrosion that occurs at the interphase of bcc and hcp phase boundaries in Ti-6Al-4V alloy can accelerate the dissolving rate of the passivation film [33]. The results of the corrosion test in NaCl solution are as follows: (1) the quaternary TiNbTaZr films presented higher corrosion resistance than that of the ternary TiNbTa films, (2) the Ti-enriched Ti₆₁Nb₁₃Ta₁₁Zr₁₅ film revealed a corrosion resistance slightly higher than that of the bare Ti-6Al-4V, and (3) the Zr-enriched Ti₁₉Nb₁₀Ta₉Zr₆₂ film revealed pitting behavior. Therefore, the Ti-6Al-4V modified with Ti₃₃Nb₁₉Ta₂₁Zr₂₇, Ti₁₅Nb₆₈Ta₈Zr₉, and Ti₈Nb₈Ta₇₉Zr₅ films should be suitable assemblies for biocompatible implantation in this study, and their high oxidation resistance was attributed to the formation of the stable passivation film on the single-bcc-phase film.

3.4. Elution Test and Formation of Surficial Oxide Layers

Figure 5 shows the images of water contact angles between the water drop and the TiNbTa(Zr) films and bare Ti-6Al-4V substrate. The contact angle was 50° for the Ti-6Al-4V substrate, which was comparable to the 55° contact angle reported in a previous study [36]. With a hydrophilic surface, the Ti-6Al-4V alloy enhanced the adsorption of human osteoblast cells and subsequent cell growth. The contact angles were 85° for the Ti₈₃Nb₁₀Ta₇, Ti₃₈Nb₃₀Ta₃₂, and Ti₁₀Nb₈₀Ta₁₀ films, whereas the Ti₁₂Nb₄Ta₈₄ film exhibited a lower contact angle of 77°. The passive oxide films formed on the metallic surfaces affected the water contact angle values by changing the surface energies [37]. Though the contact angles increased after the Ti-6Al-4V alloy was covered with TiNbTa films, these samples remained hydrophilic. The contact angles of Ti₆₁Nb₁₃Ta₁₁Zr₁₅, Ti₃₃Nb₁₉Ta₂₁Zr₂₇, Ti₁₅Nb₆₈Ta₈Zr₉, Ti₁₉Nb₁₀Ta₉Zr₆₂, and Ti₈Nb₈Ta₇₉Zr₅ film were 70°, 61°, 75°, 72°, and 70°, respectively, which were lower than those of the TiNbTa films.

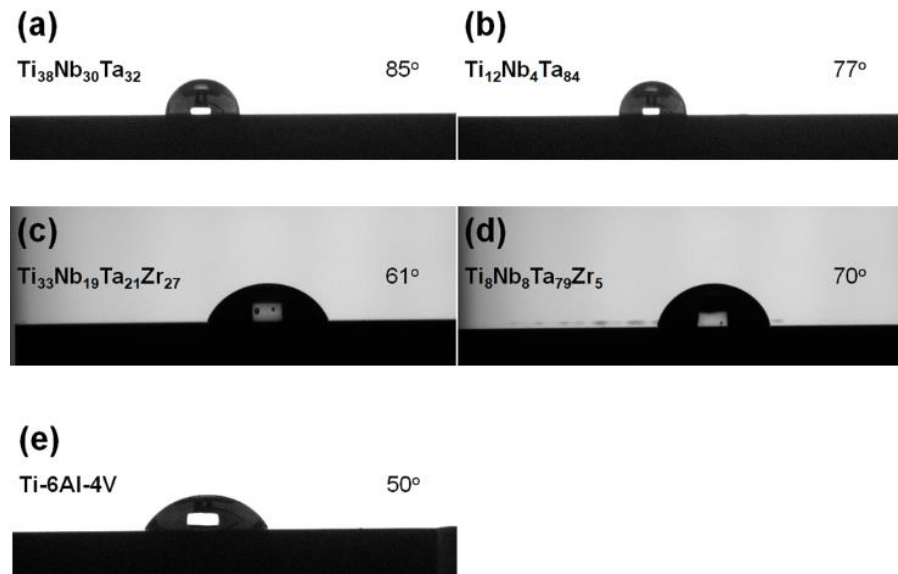


Figure 5. Water contact angles on (a) $\text{Ti}_{38}\text{Nb}_{30}\text{Ta}_{32}$, (b) $\text{Ti}_{12}\text{Nb}_4\text{Ta}_{84}$, (c) $\text{Ti}_{33}\text{Nb}_{19}\text{Ta}_{21}\text{Zr}_{27}$, and (d) $\text{Ti}_8\text{Nb}_8\text{Ta}_{79}\text{Zr}_5$ films and (e) bare Ti-6Al-4V substrate.

Figure 6a depicts the XTEM image of the $\text{Ti}_{33}\text{Nb}_{19}\text{Ta}_{21}\text{Zr}_{27}$ film after immersion in Ringer’s solution for eight weeks. The $\text{Ti}_{33}\text{Nb}_{19}\text{Ta}_{21}\text{Zr}_{27}$ film exhibited a typical columnar structure and the SAED pattern exhibited a bcc structure (Figure 6b). Figure 6c displays the HRTEM image at the near-surface region. An amorphous oxide layer of approximately 10 nm thickness was observed at the free surface. No evident lattice fringes were observed in the amorphous oxide layer. Crystalline domains with d -spacing values of 0.234–0.235 nm were observed beneath the oxide layer, which represented the bcc (110) planes.

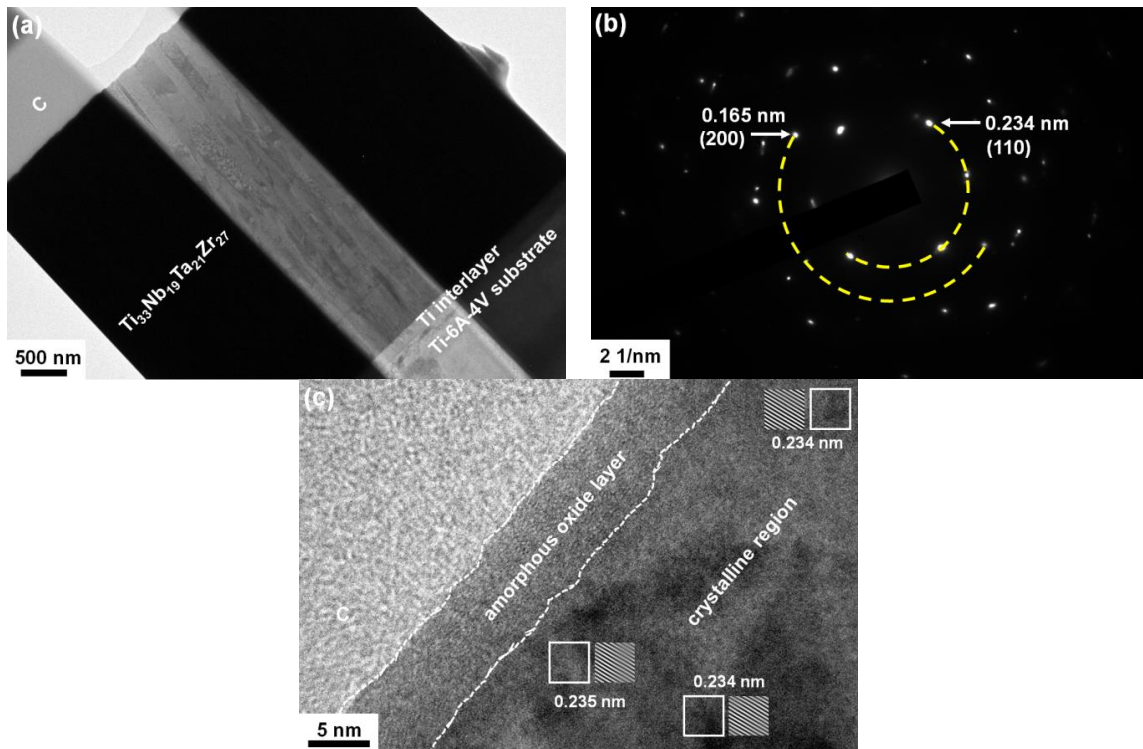


Figure 6. (a) XTEM image, (b) SAED pattern, and (c) HRTEM image of the $\text{Ti}_{33}\text{Nb}_{19}\text{Ta}_{21}\text{Zr}_{27}$ film after immersion in Ringer’s solution for eight weeks.

Figure 7 shows the compositional profiles of the TiNbTa and TiNbTaZr films examined by XPS after these samples were immersed in Ringer's solutions for eight weeks. The near-equiatomic $\text{Ti}_{38}\text{Nb}_{30}\text{Ta}_{32}$ and $\text{Ti}_{33}\text{Nb}_{19}\text{Ta}_{21}\text{Zr}_{27}$ films exhibited inward diffusion of O and Al during the elution test (Figure 7a,b). The O contents of the $\text{Ti}_{38}\text{Nb}_{30}\text{Ta}_{32}$ and $\text{Ti}_{33}\text{Nb}_{19}\text{Ta}_{21}\text{Zr}_{27}$ films exhibited a common decreasing trend with an increase in the film depth. The presence of Al at the near-surface regions of 0–7.8 nm and 0–11.7 nm for the $\text{Ti}_{38}\text{Nb}_{30}\text{Ta}_{32}$ and $\text{Ti}_{33}\text{Nb}_{19}\text{Ta}_{21}\text{Zr}_{27}$ films, respectively, resulted from the inward diffusion of Al ions from the Ringer's solution. Beneath the near-surface regions, no Al or V atoms were observed, which implies that the $\text{Ti}_{38}\text{Nb}_{30}\text{Ta}_{32}$ and $\text{Ti}_{33}\text{Nb}_{19}\text{Ta}_{21}\text{Zr}_{27}$ films formed protective barriers to isolate the Ti-6Al-4V substrate. Figure 7c displays the compositional profiles of the $\text{Ti}_8\text{Nb}_8\text{Ta}_{79}\text{Zr}_5$ film. The inward diffusion of O was restricted to a shallower depth of the $\text{Ti}_8\text{Nb}_8\text{Ta}_{79}\text{Zr}_5$ film related to those of the near-equiatomic $\text{Ti}_{38}\text{Nb}_{30}\text{Ta}_{32}$ and $\text{Ti}_{33}\text{Nb}_{19}\text{Ta}_{21}\text{Zr}_{27}$ films, which implies a higher oxidation resistance due to the formation of Ta_2O_5 . In contrast, O diffused into the Ti-6Al-4V substrate (Figure 7d), which was attributed to the lack of a passivation oxide film such as Ta_2O_5 and Nb_2O_5 [3].

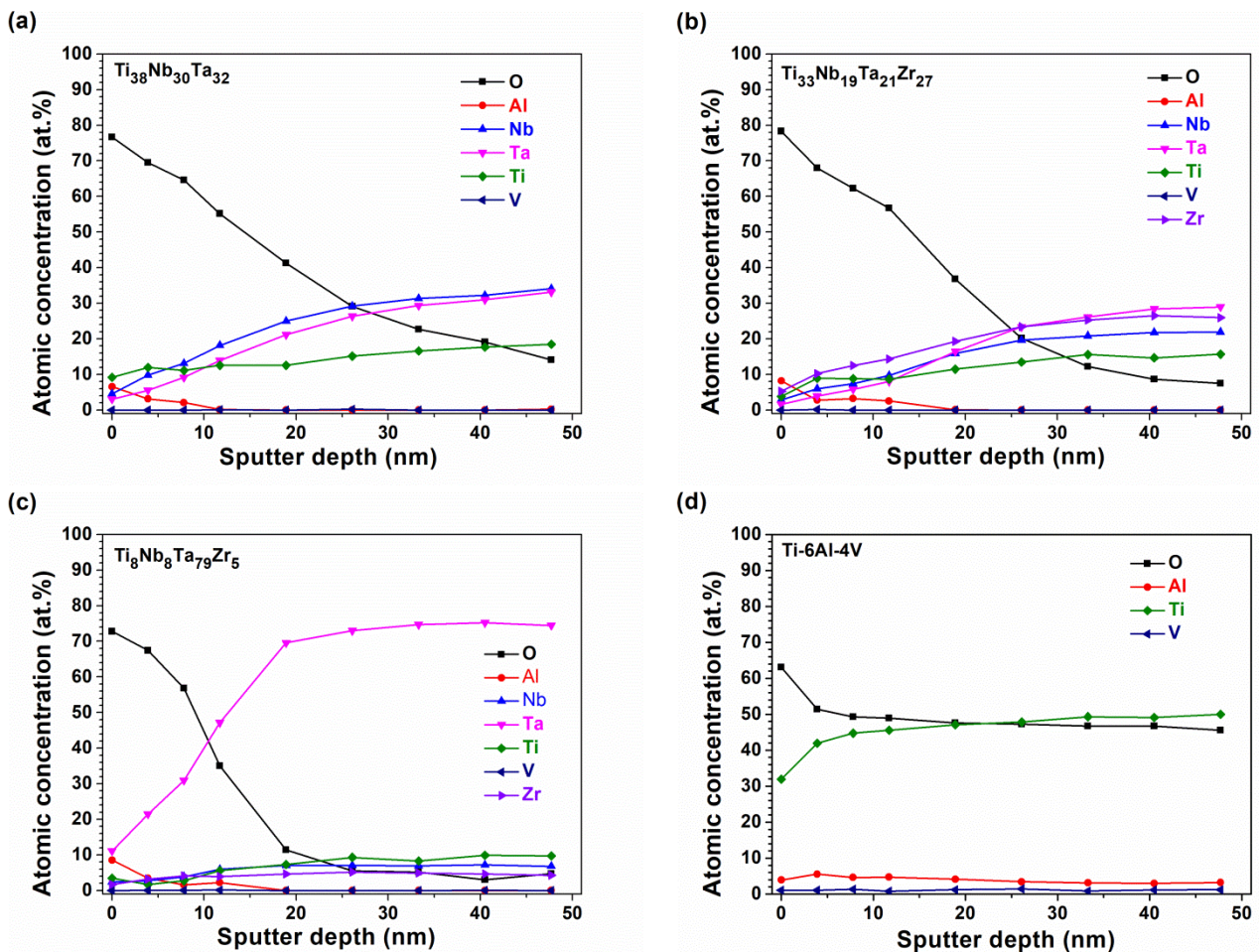


Figure 7. Compositional profiles of (a) $\text{Ti}_{38}\text{Nb}_{30}\text{Ta}_{32}$, (b) $\text{Ti}_{33}\text{Nb}_{19}\text{Ta}_{21}\text{Zr}_{27}$, and (c) $\text{Ti}_8\text{Nb}_8\text{Ta}_{79}\text{Zr}_5$ films and (d) Ti-6Al-4V substrate examined by XPS after immersion in Ringer's solution for eight weeks.

Figure 8 depicts the XPS profiles of the $\text{Ti}_{38}\text{Nb}_{30}\text{Ta}_{32}$ film at depths of 0, 7.8, and 47.7 nm after immersion in Ringer's solution for eight weeks. The splitting energies were 5.54, 2.72, and 1.91 eV for Ti 2p, Nb 3d, and Ta 4f doublets [38], respectively. The area ratios were set as 2:1, 3:2, and 4:3 for $2p_{3/2}:2p_{1/2}$, $3d_{5/2}:3d_{3/2}$, and $4f_{7/2}:4f_{5/2}$, respectively. On the free surface, binding energies of 456.55, 205.23, 24.27, and 72.50 eV indicated the signals of Ti $2p_{3/2}$ in a TiO_2 form, Nb $3d_{5/2}$ in a Nb_2O_5 form, Ta $4f_{7/2}$ in a TaO_2 form, and Al 1s in

a Al_2O_3 form, respectively. The $\text{Ti}^{4+} 2p_{3/2}$ signal exhibited a shift of -2.25 eV related to 458.8 eV shown in the handbook [38]. The FWHM values of $\text{Ti}^{4+} 2p_{3/2}$ and $2p_{1/2}$ were 1.31 and 2.20 eV, respectively. A wider FWHM value for $\text{Ti} 2p_{1/2}$ than that for the $\text{Ti} 2p_{3/2}$ that has been reported in the literature [39,40]. The aforementioned FWHM ratio was sustained for analyzing the other Ti doublets in this study. In contrast, both the FWHM ratios of $3d_{5/2}:3d_{3/2}$ and $4f_{7/2}:4f_{5/2}$ for Nb and Ta doublets, respectively, were set as 1:1. At a depth of 7.8 nm beneath the free surface, the Ti signal consisted of Ti^{4+} , Ti^{3+} , and Ti^{2+} doublets, the Nb signal consisted of Nb^{5+} , Nb^{4+} , Nb^{2+} , and Nb^0 doublets, and the Ta signal consisted of Ta^{5+} , Ta^{4+} , Ta^{2+} , and Ta^0 doublets, whereas the Al signal was not obvious. At a depth of 47.7 nm, only Ti^{2+} , Ti^0 , Nb^{2+} , Nb^0 , Ta^{2+} , and Ta^0 doublets were observed, and no Al signal was detectable. The decrease in the intensity of Al signals along the depth direction of the $\text{Ti}_{38}\text{Nb}_{30}\text{Ta}_{32}$ film suggested that the Al ions were contributed from the Ringer's solution during the elution test as examined from the compositional profiles (Figure 7). The decrease in O content in the depth direction of the $\text{Ti}_{38}\text{Nb}_{30}\text{Ta}_{32}$ film (Figure 7a) resulted in the elements of the $\text{Ti}_{38}\text{Nb}_{30}\text{Ta}_{32}$ film varying from full oxidation at the free surface to a mixture with various oxidation states and to the state being dominated with metallic atoms accompanied by minor amounts of divalent ions. Figure 9 exhibits the XPS depth profiles of the Ti-6Al-4V substrate after immersion in Ringer's solution for eight weeks. The shift of $\text{Ti}^{4+} 2p_{3/2}$ signal was -2.61 eV in relation to 458.8 eV. A Ti^{4+} doublet was observed at the free surface and depths of 7.8 and 47.7 nm, whereas a minor Ti^{3+} doublet was examined at a depth of 47.7 nm. Both the Al bondings in Al_2O_3 and Al-halides [38] were detected. These Al atoms were eluted from the bare Ti-6Al-4V substrate without protective films.

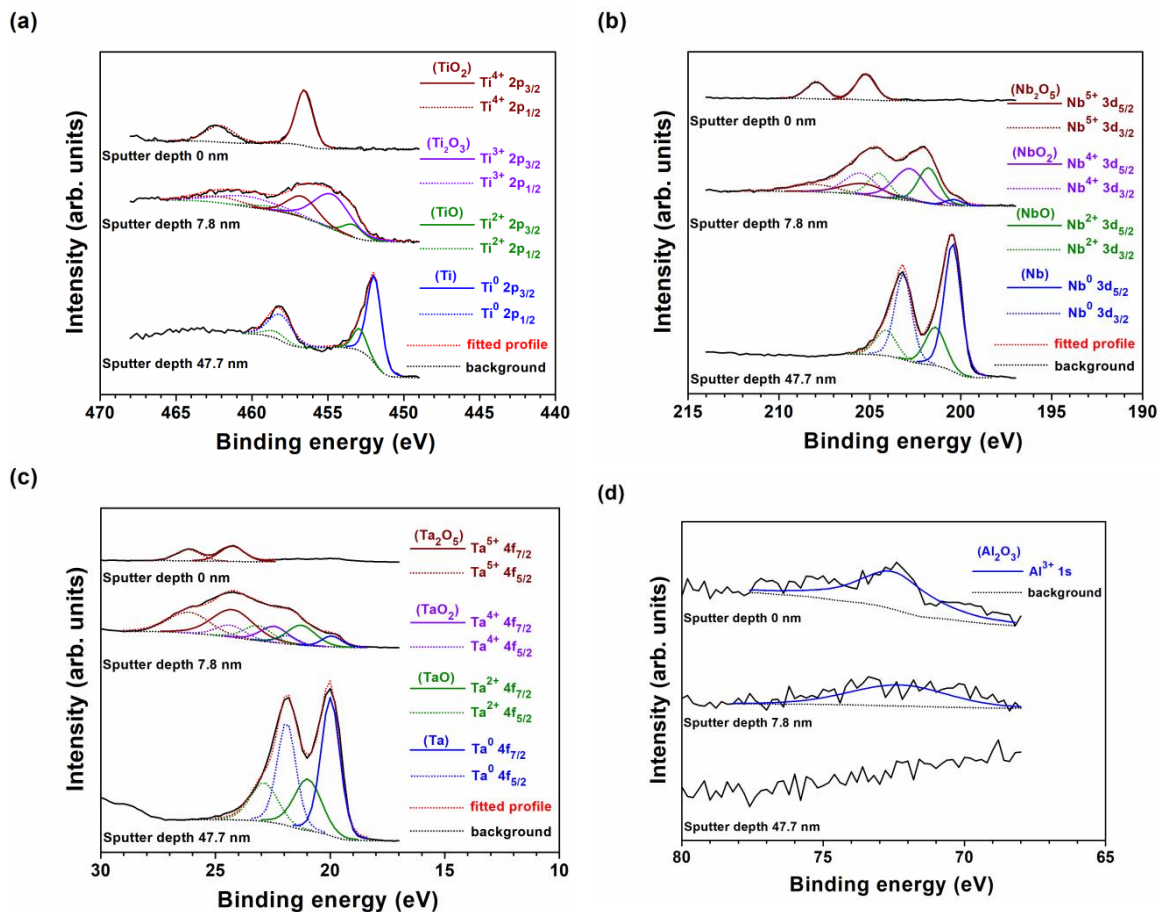


Figure 8. XPS analysis results of (a) Ti, (b) Nb, (c) Ta, and (d) Al profiles at depths of 0, 7.8, and 47.7 nm of the $\text{Ti}_{38}\text{Nb}_{30}\text{Ta}_{32}$ film after immersion in Ringer's solution for eight weeks.

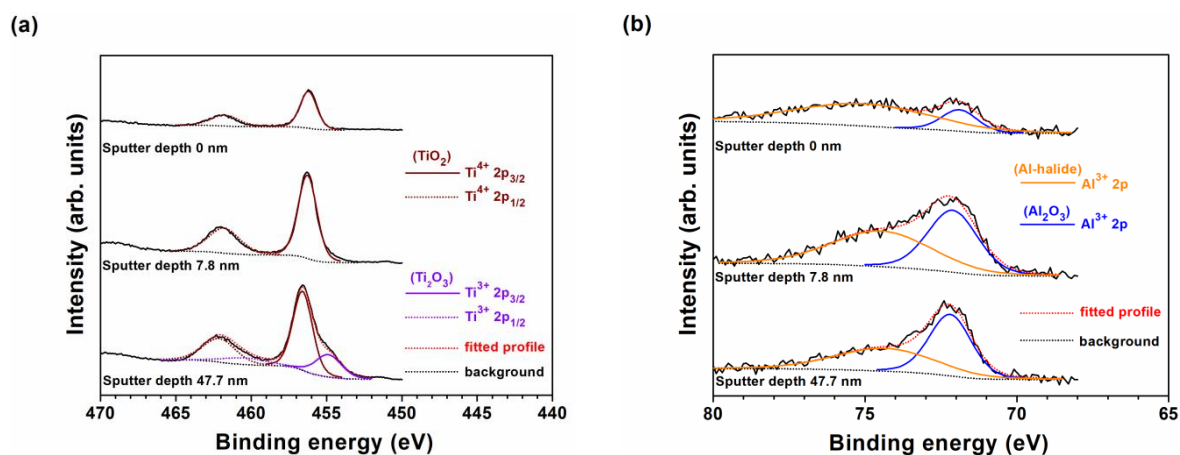


Figure 9. XPS analysis results of (a) Ti and (b) Al profiles at depths of 0, 7.8, and 47.7 nm of the Ti-6Al-4V substrate after immersion in Ringer's solution for eight weeks.

4. Conclusions

The assemblies of TiNbTa(Zr) films/Ti-6Al-4V alloys utilized as biocompatible implant materials were evaluated in this study. The chemical compositions of the TiNbTa(Zr) films were regulated through co-sputtering with four sputter sources. The phase constitutions of TiNbTa(Zr) films were correlated to their VEC values. The TiNbTa(Zr) films with a VEC value of 4.17–4.24 exhibited a mixture of hcp and bcc phases, whereas the films with a VEC value of 4.40–4.90 revealed a single bcc phase. The solid solution strengthening mechanism dominated the hardness of these TiNbTa(Zr) films. In contrast to the performance of bulk Ti alloys, β -phase TiNbTa(Zr) films exhibited Young's modulus values of 142–226 GPa, which were higher than those (108–115 GPa) of the films with an α - β mixed phase. The corrosion test in a 3.5 wt.% NaCl aqueous solution indicated that the $\text{Ti}_{33}\text{Nb}_{19}\text{Ta}_{21}\text{Zr}_{27}$, $\text{Ti}_{15}\text{Nb}_{68}\text{Ta}_8\text{Zr}_9$, and $\text{Ti}_8\text{Nb}_8\text{Ta}_{79}\text{Zr}_5$ films exhibited high anticorrosive properties deriving from the stable passivation film comprising constitutions of Ta_2O_5 , Nb_2O_5 , and ZrO_2 . The water contact angles of TiNbTaZr films were lower than those of the TiNbTa films, which implies that the TiNbTaZr films were more hydrophilic. The XPS depth profiles indicated that the elution of Al atoms from the Ti-6Al-4V alloy was inhibited by the TiNbTa(Zr) films as the TiNbTa(Zr)/Ti-6Al-4V assemblies were immersed in Ringer's solution at 310 K for eight weeks, which was attributed to the formation of an amorphous surficial oxide layer consisting of Ta_2O_5 and Nb_2O_5 . In summary, the $\text{Ti}_{33}\text{Nb}_{19}\text{Ta}_{21}\text{Zr}_{27}$, $\text{Ti}_{15}\text{Nb}_{68}\text{Ta}_8\text{Zr}_9$, and $\text{Ti}_8\text{Nb}_8\text{Ta}_{79}\text{Zr}_5$ films are suitable candidates for protective coatings on Ti-6Al-4V alloys when applied as biocompatible materials.

Author Contributions: Conceptualization, Y.-J.C. and Y.-I.C.; funding acquisition, Y.-I.C. and L.-C.C.; investigation, C.-Y.L. and Y.-J.C.; resources, Y.-I.C. and L.-C.C.; validation, C.-Y.L.; visualization, C.-Y.L.; writing—original draft preparation, C.-Y.L.; writing—review and editing, Y.-I.C. All authors have read and agreed to the published version of the manuscript.

Funding: This research was funded by the Ministry of Science and Technology, Taiwan, grant numbers 110-2221-E-019-015 and 110-2221-E-131-013. The APC was funded by National Taiwan Ocean University.

Institutional Review Board Statement: Not applicable.

Informed Consent Statement: Not applicable.

Data Availability Statement: Not applicable.

Acknowledgments: The authors thank the Instrumentation Center at the National Tsing Hua University for EPMA and XPS analyses and the Joint Center for High Valued Instruments at NSYSU for the FIB operation.

Conflicts of Interest: The authors declare no conflict of interest.

References

1. Rodil, S.E.; Olivares, R.; Arzate, H.; Muhl, S. Properties of carbon films and their biocompatibility using in-vitro tests. *Diam. Relat. Mater.* **2003**, *12*, 931–937. [[CrossRef](#)]
2. Sharma, A.; Oh, M.C.; Kim, J.-T.; Srivastava, A.K.; Ahn, B. Investigation of electrochemical corrosion behavior of additive manufactured Ti–6Al–4V alloy for medical implants in different electrolytes. *J. Alloys Compd.* **2020**, *830*, 154620. [[CrossRef](#)]
3. Hussein, A.H.; Gepreel, M.A.; Gouda, M.K.; Hefnawy, A.M.; Kandil, S.H. Biocompatibility of new Ti–Nb–Ta base alloys. *Mater. Sci. Eng. C* **2016**, *61*, 574–578. [[CrossRef](#)] [[PubMed](#)]
4. Williams, D.F. On the mechanisms of biocompatibility. *Biomaterials* **2008**, *29*, 2941–2953. [[CrossRef](#)]
5. Van Lenthe, G.H.; de Waal Malefijt, M.C.; Huijkes, R. Stress shielding after total knee replacement may cause bone resorption in the distal femur. *J. Bone Joint Surg.* **1997**, *79*, 117–122. [[CrossRef](#)]
6. Niinomi, M.; Nakai, M. Titanium-based biomaterials for preventing stress shielding between implant devices and bone. *Int. J. Biomater.* **2011**, *2011*, 836587. [[CrossRef](#)] [[PubMed](#)]
7. Huijkes, R.; Weinans, H.; Rietbergen, B.V. The relationship between stress shielding and bone resorption around total hip stems and the effects of flexible materials. *Clin. Orthop. Relat. Res.* **1992**, *274*, 124–134. [[CrossRef](#)]
8. Glassman, A.H.; Bobyn, J.D.; Tanzer, M. New femoral designs: Do they influence stress shielding? *Clin. Orthop. Relat. Res.* **2006**, *453*, 64–74. [[CrossRef](#)] [[PubMed](#)]
9. Nagels, J.; Stokdijk, M.; Rozing, P.M. Stress shielding and bone resorption in shoulder arthroplasty. *J. Shoulder Elbow Surg.* **2003**, *12*, 35–39. [[CrossRef](#)]
10. Vilhena, L.M.; Shumayal, A.; Ramalho, A.; Ferreira, J.A.M. Tribocorrosion behaviour of Ti6Al4V produced by selective laser melting for dental implants. *Lubricants* **2020**, *8*, 22. [[CrossRef](#)]
11. Fellah, M.; Labaiz, M.; Assala, O.; Dekhil, L.; Taleb, A.; Rezag, H.; Iost, A. Tribological behavior of Ti-6Al-4V and Ti-6Al-7Nb alloys for total hip prosthesis. *Adv. Tribol.* **2014**, *2014*, 451387. [[CrossRef](#)]
12. Kuroda, D.; Niinomi, M.; Morinaga, M.; Kato, Y.; Yashiro, T. Design and mechanical properties of new β type titanium alloys for implant materials. *Mater. Sci. Eng. A* **1998**, *243*, 244–249. [[CrossRef](#)]
13. Zaffe, D.; Bertoldi, C.; Consolo, U. Accumulation of aluminum in lamellar bone after implantation of titanium plates, Ti–6Al–4V screws, hydroxyapatite granules. *Biomaterials* **2004**, *25*, 3837–3844. [[CrossRef](#)] [[PubMed](#)]
14. Raabe, D.; Sander, B.; Friák, M.; Ma, D.; Neugebauer, J. Theory-guided bottom-up design of β -titanium alloys as biomaterials based on first principles calculations: Theory and experiments. *Acta Mater.* **2007**, *55*, 4475–4487. [[CrossRef](#)]
15. Song, Y.; Xu, D.S.; Yang, R.; Li, D.; Wu, W.T.; Guo, Z.X. Theoretical study of the effects of alloying elements on the strength and modulus of β -type bio-titanium alloys. *Mater. Sci. Eng. A* **1999**, *260*, 269–274. [[CrossRef](#)]
16. Niinomi, M.; Kuroda, D.; Fukunaga, K.; Morinaga, M.; Kato, Y.; Yashiro, T.; Suzuki, A. Corrosion wear fracture of new β type biomedical titanium alloys. *Mater. Sci. Eng. A* **1999**, *263*, 193–199. [[CrossRef](#)]
17. Biesiekierski, A.; Wang, J.; Gepreel, M.A.; Wen, C. A new look at biomedical Ti-based shape memory alloys. *Acta Biomater.* **2012**, *8*, 1661–1669. [[CrossRef](#)]
18. Chen, Y.H.; Chuang, W.S.; Huang, J.C.; Wang, X.; Chou, H.S.; Lai, Y.J.; Lin, P.H. On the bio-corrosion and biocompatibility of TiTaNb medium entropy alloy films. *Appl. Surf. Sci.* **2020**, *508*, 145307. [[CrossRef](#)]
19. Lai, B.-W.; Chang, Y.-Y.; Shieh, T.-M.; Huang, H.-L. Biocompatibility and microstructure-based stress analyses of TiNbZrTa composite films. *Materials* **2022**, *15*, 29. [[CrossRef](#)]
20. Tüten, N.; Canadinc, D.; Motallebzadeh, A.; Bal, B. Microstructure and tribological properties of TiTaHfNbZr high entropy alloy coatings deposited on Ti–6Al–4V substrates. *Intermetallics* **2019**, *105*, 99–106. [[CrossRef](#)]
21. Peighambardoust, N.S.; Alamdari, A.A.; Unal, U.; Motallebzadeh, A. In vitro biocompatibility evaluation of Ti_{1.5}ZrTa_{0.5}Nb_{0.5}Hf_{0.5} refractory high-entropy alloy film for orthopedic implants: Microstructural, mechanical properties and corrosion behavior. *J. Alloys Compd.* **2021**, *883*, 160786. [[CrossRef](#)]
22. Chen, Y.I.; Chen, C.Y.; Chang, L.C.; Kai, W. Characterization of cosputtered NbTaMoW films. *J. Mater. Res. Technol.* **2021**, *15*, 1090–1099. [[CrossRef](#)]
23. Cullity, B.D.; Stock, S.R. *Elements of X-ray Diffraction*, 3rd ed.; Prentice-Hall: Hoboken, NJ, USA, 2001.
24. Guo, S.; Ng, C.; Lu, J.; Liu, C.T. Effect of valence electron concentration on stability of fcc or bcc phase in high entropy alloys. *J. Appl. Phys.* **2011**, *109*, 103505. [[CrossRef](#)]
25. Yuan, Y.; Wu, Y.; Yang, Z.; Liang, X.; Lei, Z.; Huang, H.; Wang, H.; Liu, X.; An, K.; Wu, W.; et al. Formation, structure and properties of biocompatible TiZrHfNbTa high-entropy alloys. *Mater. Res. Lett.* **2019**, *7*, 225–231. [[CrossRef](#)]
26. Han, G.; Lu, X.; Xia, Q.; Lei, B.; Yan, Y.; Shang, C.J. Face-centered-cubic titanium - A new crystal structure of Ti in a Ti-8Mo-6Fe alloy. *J. Alloys Compd.* **2018**, *748*, 943–952. [[CrossRef](#)]
27. Hua, K.; Zhang, Y.; Kou, H.; Li, J.; Gan, W.; Funderberger, J.J.; Esling, C. Composite structure of α phase in metastable β Ti alloys induced by lattice strain during β to α phase transformation. *Acta Mater.* **2017**, *132*, 307–326. [[CrossRef](#)]
28. Miura, K.; Yamada, N.; Hanada, S.; Jung, T.-K.; Itoi, E. The bone tissue compatibility of a new Ti–Nb–Sn alloy with a low Young's modulus. *Acta Biomater.* **2011**, *7*, 2320–2326. [[CrossRef](#)]
29. Song, B.; Li, Y.; Cong, Z.; Li, Y.; Song, Z.; Chen, J. Effects of deposition temperature on the nanomechanical properties of refractory high entropy TaNbHfZr films. *J. Alloys Compd.* **2019**, *797*, 1025–1030. [[CrossRef](#)]

30. Pogrebnjak, A.D.; Beresnev, V.M.; Bondar, O.V.; Postolnyi, B.O.; Zaleski, K.; Coy, E.; Jurga, S.; Lisovenko, M.O.; Konarski, P.; Rebouta, L.; et al. Superhard CrN/MoN coatings with multilayer architecture. *Mater. Des.* **2018**, *153*, 47–59. [[CrossRef](#)]
31. Musil, J. Hard nanocomposite coatings: Thermal stability, oxidation resistance and toughness. *Surf. Coat. Technol.* **2012**, *207*, 50–65. [[CrossRef](#)]
32. Stern, M. A method for determining corrosion rates from linear polarization data. *Corrosion* **1958**, *14*, 60–64. [[CrossRef](#)]
33. Ji, P.F.; Li, B.; Chen, B.H.; Wang, F.; Ma, W.; Zhang, X.Y.; Ma, M.Z.; Liu, R.P. Effect of Nb addition on the stability and biological corrosion resistance of Ti-Zr alloy passivation films. *Corros. Sci.* **2020**, *170*, 108696. [[CrossRef](#)]
34. Alves, V.A.; Reis, R.Q.; Santos, I.C.B.; Souza, D.G.; de F. Gonçalves, T.; Pereira-da-Silva, M.A.; Rossi, A.; da Silva, L.A. In situ impedance spectroscopy study of the electrochemical corrosion of Ti and Ti–6Al–4V in simulated body fluid at 25 °C and 37 °C. *Corros. Sci.* **2009**, *51*, 2473–2482. [[CrossRef](#)]
35. Jiang, Z.; Dai, X.; Norby, T.; Middleton, H. Investigation of pitting resistance of titanium based on a modified point defect model. *Corros. Sci.* **2011**, *53*, 815–821. [[CrossRef](#)]
36. Mirhosseini, N.; Crouse, P.L.; Schmidh, M.J.J.; Li, L.; Garrod, D. Laser surface micro-texturing of Ti–6Al–4V substrates for improved cell integration. *Appl. Surf. Sci.* **2007**, *253*, 7738–7743. [[CrossRef](#)]
37. Razazzadeh, A.; Atapour, M.; Enayati, M.H. Corrosion characteristics of TiNbMoMnFe high entropy thin film deposited on AISI316L for biomedical applications. *Met. Mater. Int.* **2021**, *27*, 2341–2352. [[CrossRef](#)]
38. Moulder, J.F.; Stickle, W.F.; Sobol, P.E.; Bomben, K.D. *Handbook of X-ray Photoelectron Spectroscopy*; Chastain, J., King, R.C., Eds.; Physical Electronics: Chanhassen, MN, USA, 1995.
39. Krishna, D.N.G.; George, R.P.; Philip, J. Determination of nanoscale titanium oxide thin film phase composition using X-ray photoelectron spectroscopy valence band analysis. *Thin Solid Films* **2019**, *681*, 58–68. [[CrossRef](#)]
40. Chi, M.; Sun, X.; Lozano-Blanco, G.; Tatarchuk, B.J. XPS and FTIR investigations of the transient photocatalytic decomposition of surface carbon contaminants from anatase TiO₂ in UHV starved water/oxygen environments. *Appl. Surf. Sci.* **2021**, *570*, 151147. [[CrossRef](#)]